Domain Decomposition Technique with Subdomain Pre-processing in 2-D Simulations of Wireless Power Transfer

Antero Marjamäki[1] and Paavo Rasilo[2]
[1]Unit of Electrical Engineering, Tampere University, Tampere, Finland, antero.marjamaki@tuni.fi
[1]Unit of Electrical Engineering, Tampere University, Tampere, Finland, paavo.rasilo@tuni.fi

In this paper, domain decomposition is combined with a subdomain pre-processing technique to model wireless power transfer setups in which the sending and receiving coils move relative to each other. Domain decomposition is used to decouple the problem into two subdomains, which contain the coils, and a main domain, which contains the medium and the relative placement. The subdomains are dictated by the coil design, and only the main domain must be modified to vary the relative placement of the coils. Linear mappings which describe the behaviour of the subdomains in order to reduce the amount of degrees of freedom are computed. This approach greatly reduces the overall computational complexity of the repated simulation.

Index Terms—**Domain decomposition, model order reduction, wireless power transmission**

I. Introduction

WIRELESS POWER TRANSFER (WPT) systems can be utilized in charging of electric vehicles, drones, or even miniature submarines. Especially, wireless charging of moving vehicles has great potential of shaping the future in extending the ranges of electric vehicles [1].

Two big issues of wireless charging are the needs to increase power densities and mitigate the effects of displacements between the sending and receiving coils. Detailed models are needed in order to simulate these effects. These models are computationally heavy, and simulations must be run multiple times to reveal e.g. the effects of misalignment between the two coils.

In this paper, a new simulation technique is proposed, which can be used to study movement and misalignment of the coils. The main contribution is a domain decomposition technique using Fourier series and precomputed linear mappings to eliminate most of the subdomain's degrees of freedom (DOF) from the system. The technique is especially beneficial if repeated solving of the problem is required, e.g. if losses in the WPT coils caused by tilting, displacements or movement of the coils with respect to each other are simulated. A similar approach has been used in [2] to speed up electrical machine simulations by eliminating DOF of the winding slots from the system.

A 2-D cross sectional model of a rectangular WPT coil is analysed. The static coupling coefficients with different displacements and tilting angles are computed using the proposed decomposed finite-element (FE) approach. As a reference, traditional FE model is used with a mesh whose density is adjusted to be the same as in the decomposed approach.

II. Mortar Method with Lagrange Multipliers

A large global problem containing both the intermediate medium and two (or more) WPT coils is transformed into one main problem for the intermediate medium and two (or more) subproblems for the coils. A variant of the mortar method is used in which the continuity over the coupling boundaries is enforced using Lagrange multipliers [3], [4].

The challenge of this approach lies in computing of integrals of products of two functions over the boundary, when the functions are defined in different meshes. In this study, the piecewise integration of the weak form of the continuity constraint is replaced with approximate integration [5] by utilizing a Fourier series. This approach is well suited because the boundary is periodic.

A. Decomposition of the domain

Geometric models for each subdomain are first created and isometric embeddings $\iota_i : \Omega_\mathrm{S} \hookrightarrow \Omega$ are stated, which place the subdomains into the total problem domain as seen in Fig. 1. A WPT system with two identical coils in air is modeled, so only one geometrical model and two different embeddings are needed. The embeddings are used especially to map the boundaries of the subdomains into Ω. A mesh for Ω which has two holes for the subdomains is then created.

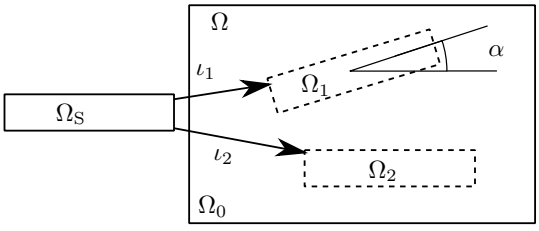

Fig. 1. The problem domain and isometric embeddings ι_1, ι_2. For the total problem domain $\Omega = \Omega_0 \cup \Omega_1 \cup \Omega_2$ holds.

The subproblems depend only on the WPT coil constructions, and the main problem can be modified to account for changes in orientation, distance, and relative movement of the coils. This approach also enables the use of meshes that differ at the common boundary of the main and subdomains.

Let's denote the total problem domain with Ω, the decomposed air domain with Ω_0, and the subdomains with Ω_1 and

Manuscript received Aug 08, 2019; revised Aug 23, 2019. Corresponding author: A. Marjamäki.

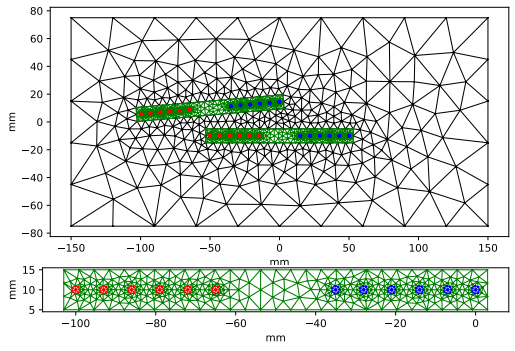

Fig. 2. An example of the meshes. The mesh of main domain Ω_0 (black) with holes where the single mesh for Ω_1 (upper) and Ω_2 (lower) is embedded two times. The conductors are colored with red and blue in the electronic version.

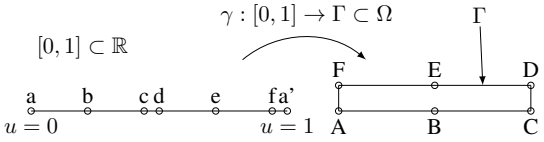

Fig. 3. The parametrization of a closed loop Γ is a mapping from the interval $[0, 1]$ to a domain Ω. The parametrized coordinates u of nodes in the mesh of Γ can be solved by first cutting the loop open by introducing an artificial node a' which along with a gets mapped to A. Then the nodal values of u can be solved from $\nabla \cdot \nabla u = 0$ with boundary conditions $u = 0$ at a and $u = 1$ at a'.

Ω_2 as seen in Fig 1. The meshes of the decomposed model problem can be seen in Fig. 2. The boundary of domain n is denoted with Γ_n, and the common boundary between domains Ω_n and Ω_m is denoted with Γ_{nm}. When the meshed domains are discussed, a distinction needs to be made between Γ_{nm} and Γ_{mn}. Hence, Γ_{nm} is used to denote the restriction of the mesh of Ω_n to the common boundary.

To construct the Fourier series used to realize the weak continuity constraints, the parametrization of the boundaries needs to be obtained. This can be done by fixing one point from the boundary as an origin and solving a 1-D Laplace problem (see Fig. 3). After obtaining the parametric coordinates, 1-D Fourier series is used to represent the fields at the boundaries.

In the following sections we show how the mortar mapping is computed for the upper coil domain Ω_1. The other case is computed similarly.

B. Decomposition of the function spaces

In this model, a static A–ϕ formulation in 2-D is used. The magnetic vector potential is denoted with A_0, A_1 and A_2 in the main domain and the subdomains, respectively. To enforce the continuity of the solution across the boundaries Γ_{10} and Γ_{20}, Lagrange multipliers are needed.

The Lagrange multiplier spaces are defined as spaces of functions spanned by a Fourier basis which is truncated by some truncation limit K

$$\mathcal{B}_K^*(\Gamma) = \text{span}\left(\{\phi_k\}_{k\in I_K}\right) \tag{1}$$

where I_K denotes the set of integers from the interval $\left[-\frac{K}{2}, \frac{K}{2}\right)$. The Fourier basis functions on the parametric domain $[0, 1)$ are defined as

$$\phi_k(u) = e^{2\pi jku} \ , \tag{2}$$

where j is the imaginary unit, $u \in [0, 1)$ is the parametric coordinate.

The continuity constraint in weak form can be expressed as

$$\int_{\Gamma_{10}} (\chi_1 A_1|_{\Gamma_{10}} - \chi_0 A_0|_{\Gamma_{01}})\, b \,\mathrm{d}u = 0 \ , \forall\, b \in \mathcal{B}_K^*(\Gamma_{10}) \ , \tag{3}$$

where χ_1, χ_0 are projection maps to $\mathcal{B}_K^*(\Gamma_{10})$ and the vector potentials $A_1|_{\Gamma_{10}}$ and $A_0|_{\Gamma_{01}}$ are restrictions of A_1 and A_0 on Γ_{10} and Γ_{01}, respectively.

Let's denote the number of nodes in the meshes of Γ_{10} and Γ_{01} with N_1 and N_0. After applying the projections and standard weak form manipulations this leads to

$$\hat{A}_1^k - \hat{A}_2^k = 0 \ , \tag{4}$$

for all $k \in I_K$ where $K = \min(N_1, N_0)$. This loosely states that the two functions are approximately equal at the boundary, if their K first Fourier coefficients are equal. If K is chosen to be less than $\min(N_1, N_0)$ some of the non-redundant frequencies are neglected. This can be done, but a further analysis of this is outside the scope of this study.

The k-th Fourier coefficient is computed as

$$\hat{A}_n^k = \int_0^1 A_n(u) e^{-2\pi jku} \mathrm{d}u \tag{5}$$

$$= \int_0^1 \sum_{i=1}^{N_\mathrm{n}} \psi_i(u) a_n^i e^{-2\pi jku} \mathrm{d}u \tag{6}$$

$$= \sum_{i=1}^{N_\mathrm{n}} a_n^i \int_0^1 \psi_i(u) e^{-2\pi jku} \mathrm{d}u \ , \tag{7}$$

where ψ_i are FE basis functions in Γ_{nm}. This can be formulated as a matrix equation

$$\hat{\mathbf{a}}_n = \mathrm{D}_{nm} \mathbf{a}_n \ , \tag{8}$$

where $\mathbf{a}_n$ is a vector of nodal values of the vector potential, $\hat{\mathbf{a}}_n$ is a vector of the Fourier coefficients, and

$$[\mathrm{D}_{nm}]_{ki} = \int_0^1 \psi_i(u) e^{-2\pi jku} \mathrm{d}u \ , \tag{9}$$

is a mapping from a field defined on Γ_{nm} to the Fourier coefficients. The elements of D_{nm} can be computed analytically for FE basis functions of different orders in the reference element. This gives a fast and accurate method to construct the matrices D_{nm}.

With the help of (4) and (8), a relationship between the nodal values of A_1 and nodal values of A_0 can be written as

$$\mathrm{D}_{10}\, \mathbf{a}_1 = \mathrm{D}_{01}\, \mathbf{a}_0 \ , \tag{10}$$

where $\mathrm{D}_{10} \in \mathbb{C}^{K\times N_1}$ and $\mathrm{D}_{01} \in \mathbb{C}^{K\times N_0}$. Equation (10) is utilized to state the continuity constraint in the matrix formulation of the coupled decomposed system presented in the following section.

C. The decomposed system

The standard FE discretization of the system in Ω yields a matrix equation

$$\mathrm{S}\mathbf{a} = \mathbf{f} \,. \tag{11}$$

Now using the mortar method approach, the domain Ω is split and weak continuity is enforced at the boundaries Γ_{10} and Γ_{20} by using Lagrange multipliers $\mathbf{b}$. The FE matrices are decomposed similarly as in Schur complement method, explained e.g in [6], to separate the parts related to the inner DOF and the boundary DOF of the domains. Equation (11) becomes

$$\begin{bmatrix} \mathrm{S} & \mathrm{D}^{\mathrm{H}} \\ \mathrm{D} & 0 \end{bmatrix} \begin{bmatrix} \mathbf{a} \\ \mathbf{b} \end{bmatrix} = \begin{bmatrix} \mathbf{f} \\ \mathbf{0} \end{bmatrix} , \tag{12}$$

where H denotes a conjugate transpose and

$$\mathrm{S} = \begin{bmatrix} \mathrm{S}_0 & 0 & 0 & 0 & 0 \\ 0 & \mathrm{S}_{11} & \mathrm{S}_{\mathrm{b}10} & 0 & 0 \\ 0 & \mathrm{S}_{\mathrm{b}10}^{\mathrm{T}} & \mathrm{S}_{\mathrm{bb},10} & 0 & 0 \\ 0 & 0 & 0 & \mathrm{S}_{22} & \mathrm{S}_{\mathrm{b}20} \\ 0 & 0 & 0 & \mathrm{S}_{\mathrm{b}20}^{\mathrm{T}} & \mathrm{S}_{\mathrm{bb},20} \end{bmatrix} , \tag{13}$$

$$\mathrm{D} = \begin{bmatrix} 0 & \mathrm{D}_{01} & 0 & 0 & -\mathrm{D}_{10} & 0 & 0 \\ 0 & 0 & \mathrm{D}_{02} & 0 & 0 & 0 & -\mathrm{D}_{20} \end{bmatrix} \tag{14}$$

are block matrices where

$$\mathrm{S}_0 = \begin{bmatrix} \mathrm{S}_{00} & \mathrm{S}_{\mathrm{b}01} & \mathrm{S}_{\mathrm{b}02} \\ \mathrm{S}_{\mathrm{b}01}^{\mathrm{T}} & \mathrm{S}_{\mathrm{bb},01} & 0 \\ \mathrm{S}_{\mathrm{b}02}^{\mathrm{T}} & 0 & \mathrm{S}_{\mathrm{bb},02} \end{bmatrix} . \tag{15}$$

Equation (12) has in total nine block rows and columns. Here matrix S_{nn} denotes the part of the stiffness matrix which is related to inner nodes in domain Ω_n, matrix $\mathrm{S}_{\mathrm{b}nm}$ denotes the part which relates to the coupling between the inner nodes and the nodes in the boundary Γ_{nm}, and matrix $\mathrm{S}_{\mathrm{bb},nm}$ denotes the part of the matrix related to the connections between the nodes at the boundary Γ_{nm}. Matrix D contains the coupling terms D_{nm} between the domains, which are the Fourier transform matrices derived in the previous section.

The state, Lagrange multiplier, and source vectors are

$$\mathbf{a} = \begin{bmatrix} \mathbf{a}_0^{\mathrm{T}} & \mathbf{a}_{\mathrm{b}01}^{\mathrm{T}} & \mathbf{a}_{\mathrm{b}02}^{\mathrm{T}} & \mathbf{a}_1^{\mathrm{T}} & \mathbf{a}_{\mathrm{b}10}^{\mathrm{T}} & \mathbf{a}_2^{\mathrm{T}} & \mathbf{a}_{\mathrm{b}20}^{\mathrm{T}} \end{bmatrix}^{\mathrm{T}} , \tag{16}$$

$$\mathbf{b} = \begin{bmatrix} \mathbf{b}_{10}^{\mathrm{T}} & \mathbf{b}_{20}^{\mathrm{T}} \end{bmatrix}^{\mathrm{T}} , \tag{17}$$

$$\mathbf{f} = \begin{bmatrix} 0 & 0 & 0 & \mathrm{C}_1^{\mathrm{T}} I_1 & 0 & \mathrm{C}_2^{\mathrm{T}} I_2 & 0 \end{bmatrix}^{\mathrm{T}} , \tag{18}$$

which are written in the transpose form for brevity and where $\mathbf{a}_n$ are the inner nodal values in the domain n, $\mathbf{a}_{\mathrm{b}nm}$ and $\mathbf{b}_{nm}$ are the nodal values and the Lagrange multipliers in boundary Γ_{nm}, respectively, C_n is a mapping which distributes the source current into the conducting domains, and I_n are the source currents.

III. Pre-processing of the subdomains

The pre-processing is done by following the Schur complement method. From the fourth and the sixth row of the total system described in form in (12) first $\mathbf{a}_n$ and then $\mathrm{S}_{\mathrm{b}n}^{\mathrm{T}}\mathbf{a}_n$ can be solved as a function of $\mathbf{a}_{\mathrm{b}n0}$ and current I_n.

$$\begin{aligned} \mathrm{S}_{\mathrm{b}n0}^{\mathrm{T}}\mathbf{a}_n &= -\mathrm{S}_{\mathrm{b}n0}^{\mathrm{T}}\mathrm{S}_{nn}^{-1}\mathrm{S}_{\mathrm{b}n0}\,\mathbf{a}_{\mathrm{b}n0} + \mathrm{S}_{\mathrm{b}n0}^{\mathrm{T}}\mathrm{S}_{nn}^{-1}\mathrm{C}_n\,I_n & (19)\\ &= \mathrm{L}_{\mathrm{b}n}\,\mathbf{a}_{\mathrm{b}n0} + \mathrm{L}_{\mathrm{I}n}\,I_n \,, & (20) \end{aligned}$$

where $\mathrm{L}_{\mathrm{b}n} = -\mathrm{S}_{\mathrm{b}n0}^{\mathrm{T}}\mathrm{S}_{nn}^{-1}\mathrm{S}_{\mathrm{b}n0}$ and $\mathrm{L}_{\mathrm{I}n} = \mathrm{S}_{\mathrm{b}n0}^{\mathrm{T}}\mathrm{S}_{nn}^{-1}\mathrm{C}_n$. The computation involves solving $N_n + 1$ equations, one for each column of $\mathrm{S}_{\mathrm{b}n0}$ and one for the current. It is beneficial to factorize S_{nn} to do the repeated solving efficiently.

Now (20) can be inserted to the fifth and seventh block rows of (12), and the fourth and sixth block rows can be eliminated entirely. After this matrices S and D become

$$\mathrm{S} = \begin{bmatrix} \mathrm{S}_0 & 0 & 0 \\ 0 & \mathrm{L}_{\mathrm{b}1} + \mathrm{S}_{\mathrm{bb},10} & 0 \\ 0 & 0 & \mathrm{L}_{\mathrm{b}2} + \mathrm{S}_{\mathrm{bb},20} \end{bmatrix} , \tag{21}$$

$$\mathrm{D} = \begin{bmatrix} 0 & \mathrm{D}_{01} & 0 & -\mathrm{D}_{10} & 0 \\ 0 & 0 & \mathrm{D}_{02} & 0 & -\mathrm{D}_{20} \end{bmatrix} \tag{22}$$

and $\mathbf{a}$, $\mathbf{b}$, and $\mathbf{f}$ become

$$\mathbf{a} = \begin{bmatrix} \mathbf{a}_0^{\mathrm{T}} & \mathbf{a}_{\mathrm{b}01}^{\mathrm{T}} & \mathbf{a}_{\mathrm{b}02}^{\mathrm{T}} & \mathbf{a}_{\mathrm{b}10}^{\mathrm{T}} & \mathbf{a}_{\mathrm{b}20}^{\mathrm{T}} \end{bmatrix}^{\mathrm{T}} , \tag{23}$$

$$\mathbf{b} = \begin{bmatrix} \mathbf{b}_{10}^{\mathrm{T}} & \mathbf{b}_{20}^{\mathrm{T}} \end{bmatrix}^{\mathrm{T}} , \tag{24}$$

$$\mathbf{f} = \begin{bmatrix} 0 & 0 & 0 & -\mathrm{L}_{\mathrm{I}1}^{\mathrm{T}} I_1 & -\mathrm{L}_{\mathrm{I}2}^{\mathrm{T}} I_2 \end{bmatrix}^{\mathrm{T}} . \tag{25}$$

As a result of the elimination, two dense blocks are introduced into the matrix S. This increases the amount of nonzero elements and makes the solution process slower than solving a sparse system, if the amount of eliminated DOF is not high enough compared to the amound of DOF on the boundary. However if the winding contains any detailed structure, such as multilayer windings of litz-wires, this process will yield shorter solution times and reduce the memory consumption.

The flux linkage of the coil n can be computed from the nodal values of the full subdomain vector potential as

$$\Phi_n = \mathrm{C}_n^{\mathrm{T}}\mathbf{a}_n \,, \tag{26}$$

where

$$[\mathrm{C}_n]_i = \frac{1}{S_n}\int_{\Omega_{nc}} N_i(x,y)\,\mathrm{d}x\mathrm{d}y \;\in \mathbb{R}^{N_\mathrm{f}}, \tag{27}$$

where Ω_{nc} denotes the domain of the conductors in the windings, and S_n is the area of the domain. The flux linkage can be computed from the boundary solution and the input current by

$$\Phi_n = \mathrm{C}_n^{\mathrm{T}}\mathrm{S}_{nn}^{-1}\mathrm{S}_{\mathrm{b}n}\mathbf{a}_{\mathrm{b}n} + \mathrm{C}_n^{\mathrm{T}}\mathrm{S}_{nn}^{-1}\mathrm{C}_n I_n \,, \tag{28}$$

where the coefficient matrices can also be precomputed.

IV. Results

As an example, the coupling coefficient of two rectangular wireless power transfer coils with six turns is computed using a 2-D cross section model. The proposed technique was implemented using python. The geometries and meshing was handled using GMSH's [7] python API. The implementation was done in such a way that results from traditional finely-discretized single-domain and the proposed approach can be compared. The model can simulate the behaviour of changing distance, rotation angle, and displacement between the two coils. The coupling coefficient k is computed using

$$k = \frac{M}{\sqrt{L_1 L_2}} \,, \tag{29}$$

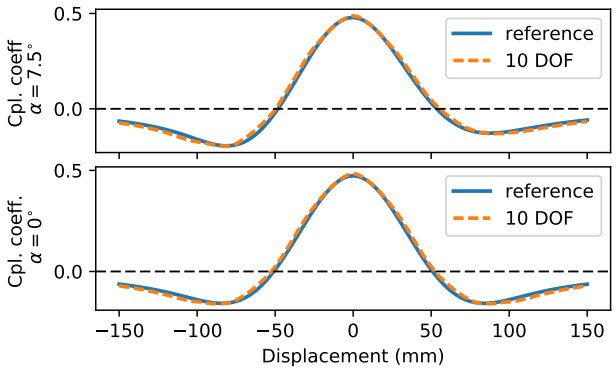

Fig. 4. The coupling coefficients obtained with different angles using the reference- and proposed approach. Reference curve is solved using 82 DOF at the boundary and the dashed curve is the worst case using 22 DOF in the coil domain side of the boundary and 10 DOF in the air domain side.

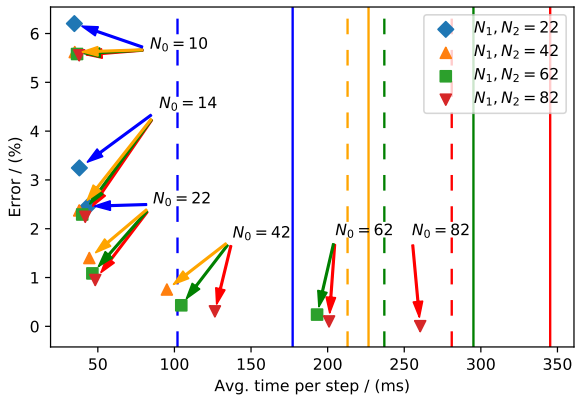

Fig. 5. Comparison between the computation time and error for the method. A preprocessed model for the coil domains with specific amount of nodes in the boundary (given by the legend) was created and the air mesh was varied. The annotations point out the amount of DOF in the air domain boundary at the datapoint. The legend shows the amount of DOF in the coil domain boundary, which stays constant throughout each data series. Solid and dashed lines show the average reference computation times and the subdomain pre-processing times, respectively. Color in electronic version.

where M is the mutual inductance and L_1 and L_2 the inductances of upper and lower coils, respectively. Computation is done in $N_\mathrm{d} = 101$ displacements along the x-axis ranging from $-150\,\mathrm{mm}$ to $150\,\mathrm{mm}$ with two angles $7.5°$ and $0°$. The results are presented in Fig. 4. Each set of parameters is simulated with varying amount of nodes in the air side boundary to demonstrate how the difference in the mesh density over the boundary affects the computation accuracy and time (see Fig. 5). The simulation times contain the re-meshing, solving and post-processing times to obtain the coupling coefficient. The pre-processing times of the subdomains are separately shown in Fig. 5.

The mesh density in the windings was approximately 100 elements per conductor in all simulations. The results of the 82 coil domain side boundary node case are shown in Table I with N_cpl nodes in the air sides of the subdomain boundaries. The first row is the reference solution.

The error of k is calculated as a relative 2-norm error over

TABLE I
RESULTS FOR 82 BOUNDARY NODE CASE.

N_cpl	DOF	nonzeros	k_r (%)	avg. time per step (ms)
82	5007	34451	ref.	343
82	2020	78170	0.01	259
42	1209	40253	0.30	129
22	811	26147	1.03	75
12	663	20665	2.83	52

the displacements

$$k_r = \sqrt{\frac{\sum_{i=1}^{N_\mathrm{d}} |k(x_i) - k_\mathrm{d}(x_i)|^2}{\sum_{j=1}^{N_\mathrm{d}} |k(x_j)|^2}}\,, \tag{30}$$

where k and k_d denote the coupling coefficients using the traditional and proposed approaches, respectively. From Fig. 5 the development of the error and speedup with respect to the densities at the boundary can be seen.

V. DISCUSSION & CONCLUSION

It can be seen from the results that using the proposed approach the amount of DOF and also the amount of nonzero elements in the total system can be made significantly smaller than in a traditional FE approach. The re-meshing of the complex geometries in the coils is avoided. This results in faster and less resource demanding simulations, especially when the simulation needs to be repeated. Approximately the same computational time is achieved regardless of the amount of DOF selected in the pre-processing stage.

Drawbacks of the Fourier approach are that the approach is only applicable to domains which have a periodic boundary and the effects of impulses at the boundary are not local. There can be artificial responses to impulses which spread through the coupling domain caused by the global Fourier basis. In practice, however, they seem to have a very small effect on the accuracy.

ACKNOWLEDGEMENT

The foundation of Emil Aaltonen and Academy of Finland are acknowledged for financial support.

REFERENCES

[1] A. Ahmad, M. Saad Alam and R. Chabaan, "A comprehensive review of wireless charging technologies for electric vehicles," *IEEE Transactions on Transportation Electrification*, vol. 4, no. 1, 2017

[2] A. Lehikoinen, J. Ikäheimo, A. Arkkio and A. Belahcen, "Domain decomposition approach for efficient time-domain finite-element computation of winding losses in electrical machines," in *IEEE Transactions on Magnetics*, vol. 53, no. 5, 2017

[3] F. B. Belgacem, "The mortar finite element method with Lagrange multipliers," in *Numerische Mathematik*, vol. 84, no. 2, 1999

[4] B. Wohlmuth, "A mortar finite element method using dual spaces for the Lagrange multiplier," in *SIAM Journal on Numerical Analysis*, vol. 38, no. 3, 2000

[5] S. Falletta, "The approximate integration in the mortar method constraint," in *Domain Decomposition Methods in Science and Engineering XVI*, 2007

[6] C. Lee, E. Kim and C. Im, "Techniques for Efficient Computation of Electric Fields Generated by Transcranial Direct-Current Stimulation," in *IEEE Transactions on Magnetics*, vol. 54, no. 5, pp. 1-5, May 2018

[7] C. Geuzaine and J.-F. Remacle, "Gmsh: a three-dimensional finite element mesh generator with built-in pre- and post-processing facilities," *International Journal for Numerical Methods in Engineering*, vol. 79, no. 11, pp. 1309-1331, 2009.